PHYSICAL REVIEW B **95**, 115433 (2017)

Wigner crystal phases in confined carbon nanotubes

L. Sárkány,[1] E. Szirmai,[1] C. P. Moca,[1,2] L. Glazman,[3] and G. Zaránd[1]
[1]*BME-MTA Exotic Quantum Phases Research Group, Institute of Physics, Budapest University of Technology and Economics, Budafoki út 8., H-1111 Budapest, Hungary*
[2]*Department of Physics, University of Oradea, 410087, Oradea, Romania*
[3]*Department of Physics, Yale University, New Haven, Connecticut 06520, USA*

(Received 18 October 2016; revised manuscript received 28 February 2017; published 27 March 2017)

We present a detailed theoretical analysis of the Wigner crystal states in confined semiconducting carbon nanotubes. We show by detailed semimicroscopic calculations that the effective exchange interaction has an SU(4) symmetry, and can reach values as large as $J \sim 100\,\mathrm{K}$ in weakly screened, small diameter nanotubes, close to the Wigner crystal—electron liquid crossover. This large value of the exchange coupling in the crossover region also follows from robust scaling arguments. Modeling the nanotube carefully and analyzing the magnetic structure of the inhomogeneous electron crystal, we recover the experimentally observed "phase boundaries" of Deshpande and Bockrath [V. V. Deshpande and M. Bockrath, Nat. Phys. **4**, 314 (2008)]. Spin-orbit coupling only slightly modifies these boundaries, but breaks the spin symmetry down to SU(2) × SU(2), and in Wigner molecules it gives rise to interesting excitation spectra, reflecting the underlying SU(4) as well as the residual SU(2) × SU(2) symmetries.

DOI: 10.1103/PhysRevB.95.115433

I. INTRODUCTION

Electrons interacting through simple Coulomb interaction represent a most fundamental, nevertheless challenging interacting quantum system. Apart from dimensionality (D), the behavior of a Coulomb gas depends on just two parameters: the temperature T, and the strength of the Coulomb interaction relative to the electrons' kinetic energy, characterized by the dimensionless ratio [1]

$$r_s = \frac{e^2 m^*}{\epsilon\,\hbar^2 n_e^{1/\mathrm{D}}}, \tag{1}$$

with n_e denoting the electron density, m^* the electrons' effective mass, and ϵ the dielectric constant of the environment through which electrons interact.

While at very high temperatures electrons form a (almost) classical plasma, the behavior of the gas at low temperatures depends on the specific value of r_s. At large densities corresponding to $r_s \ll 1$, the Coulomb interaction plays a minor role in $\mathrm{D} = 3$ dimensions, and Landau's Fermi liquid state emerges as the temperature is lowered. At small densities ($r_s \gg 1$), however, interactions become strong and relevant. In this limit, translational symmetry is broken, electrons localize at low temperatures, and form a Wigner crystal, characterized by magnetic ordering [2–4].

While the three-dimensional picture of the previous paragraph applies also to two dimensions [5–11], it fails in one dimension, where quantum fluctuations destroy the long-ranged charge order, remove the phase transition(s)[1] between the crystalline and the liquid phases, and replace it by a smooth crossover at some value $r_s \approx r^*_{1\mathrm{D}}$ [12,13]. Though there is no phase transition in one dimension, the physical picture is quite different in the dilute, $r_s \gg r^*_{1D}$, and dense regimes, $r_s \ll r^*_{1D}$. In the Wigner crystal regime, $r_s \gg r^*_{1D}$, the density-density correlation function reveals charges localized relative to each other, reflected in deep and long-ranged periodic oscillations [13–21]. In contrast, in the weakly interacting limit, $r_s \ll r^*_{1D}$, these oscillations become weak perturbations on a nonoscillating background.[2] These differences are even more pronounced in a finite system, where charges are typically pinned by some walls or confining potentials, and a true Wigner crystal structure emerges at small densities [17,22–24].

In a recent experiment, Deshpande and Bockrath reported the (indirect) observation of a Wigner crystal state in a suspended carbon nanotube with a presumably confinement induced gap [25,26]. In a finite magnetic field, they have observed oscillations in the addition energy of holes in a p-type nanotube, and argued that only a Wigner crystal picture is able to account for these oscillations systematically (see Fig. 1 for their "phase diagram"). More recently, an isolated two-electron Wigner molecule has been observed in an ultraclean carbon nanotube [27]. In the latter experiments, the observed level structure has been supported by detailed "*ab initio*" calculations, evidencing an exchange splitting much below the single particle level spacing, a clear indication of the Wigner crystal regime. In addition to these experiments, circumstantial evidence to support the formation of a Wigner crystal in one-dimensional wires has also been reported recently by other experimental groups [28–30]. It has been suggested in Ref. [28], e.g., that Wigner crystallization accounts for the negative Coulomb drag effect observed in coupled parallel quantum wires.

---

[1] Several intruding magnetic phases have been proposed, preempting a direct transition between the Wigner crystal and the Fermi liquid state.

[2] In case of screening, both regimes can be described as a Luttinger liquid. However, while the charge- and spin velocities are about the same for $r_s \ll r^*$, the spin velocity c_s gets exponentially suppressed compared to the charge velocity c_c in the Wigner crystal regime, $r_s \gg r^*$.

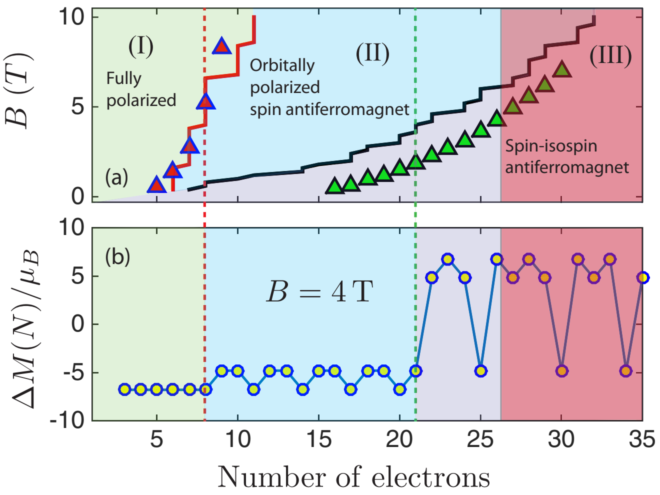

FIG. 1. (a) "Phase diagram" for an unscreened nanotube with $\epsilon = 2$ and of a radius $R = 1.6$ nm, as a function of particle number N, and external magnetic field B. Red and black curves denote the phase boundaries based upon our theoretical calculations with spin-orbit coupling, $\Delta_{\rm SO} = 0.186$ meV ($\Delta_{\rm SO} \approx 2.1$ K). The fully polarized, orbitally polarized, and unpolarized states are displayed in different colors. Green and red symbols indicate the boundaries for the experimental phase diagram of Ref. [25]. (b) Overall magnetization change at charge transitions as a function of N for $B = 4$ T. The vertical dashed lines indicate the jumps corresponding to the phase boundaries. For $N > 26$ the Wigner crystal starts to "melt". The melted region is indicated by the red shaded areas.

Although for the experiments of Ref. [25] the Wigner crystal picture seemed to provide a coherent explanation, a sufficiently "microscopic" theoretical description of the nanotube's Wigner crystal state was missing. Furthermore, in several other experiments [31,32] a single-particle or mean-field scenario, or eventually a Luttinger liquid picture appears to be sufficient [33–35]. The goal of the present work is to provide a detailed and quantitative theoretical description of an inhomogeneous Wigner crystal in a gapped carbon nanotube, to investigate its intriguing spin and pseudospin (chirality) physics, and to make a comparison with the experimental findings of Ref. [25]. For this purpose, we use a bottom-up approach. We start out from a detailed microscopic modeling of the nanotube, similar to Ref. [17], and extract the effective exchange interaction of two neighboring electrons in the Hartree field of all other electrons from their two-electron spectrum. Exchange processes involve both the spin (σ) and chiral spin (τ) of the crystallized electrons, and an almost perfectly SU(4)-symmetric exchange interaction is recovered [36,37]. We then determine the positions of the crystallized electrons self-consistently at the classical level and, having the separation dependence of the exchange coupling J in hand, arrive at an effective exchange Hamiltonian,

$$H_{\rm X} = \frac{1}{2}\sum_i J_i\, X^{\sigma}_{i,i+1} X^{\tau}_{i,i+1}, \tag{2}$$

with the operators $X^{\sigma}_{i,i+1}$ and $X^{\tau}_{i,i+1}$ exchanging the spin and the chiral spin of neighboring electrons in the crystal and $J_i = J(d_{i,i+1})$.[3] This exchange Hamiltonian is appropriate in the Wigner crystal regime, and its structure is dictated by (approximate) symmetries. In general, beyond nearest neighbor interactions as well as multispin interactions may also appear, but these terms are suppressed in the Wigner crystal regime, and therefore we neglect them here. Although the exchange Hamiltonian $H_{\rm X}$ possesses SU(4) symmetry, this symmetry is broken to SU(4) → SU(2) × SU(2) by the spin-orbit (SO) coupling [38–42]. The spin-orbit coupling between the motion of the particles around the tube and their spin can be taken into account by the term

$$H_{\rm SO} = -\frac{1}{2}\sum_{i=1}^{N} \Delta_{\rm SO}\, \sigma_i \tau_i, \tag{3}$$

with τ_i and σ_i denoting the chirality and spin of the ith localized electron, respectively, and $\Delta_{\rm SO}$ the spin-orbit splitting. We use the effective Hamiltonians (2) and (3) first to construct and classify the low-energy excitations of Wigner molecules, and then to construct the phase diagram of a parabolically confined Wigner crystal in a magnetic field by means of an inhomogeneous valence bond approach [34].

The final phase diagram, constructed from the magnetization jumps between different charging states of the nanotube is summarized in Fig. 1 (and discussed in Sec. IV). Our theoretical phase diagram compares astonishingly well with the experimentally determined phase boundaries in Ref. [25]. Our calculations rely on just a few parameters, estimated from the experimental data: the radius $R = 1.6$ nm of the nanotube, yielding the experimentally reported curvature induced gap $E_g \sim 220$ meV [43], the dielectric constant ϵ, the strength of a parabolic confinement potential α, defined in Eq. (13) and determined from the addition energy spectra (see Ref. [44] and Appendix D for details), and the measured orbital magnetic moment (g factor). We thus have one unknown parameter, the dielectric constant ϵ. The value of ϵ incorporates various screening effects including that of plasmonic excitations and, depending on the specific arrangements and the chirality of the nanotube, can take very different values [45]. Throughout this paper we use the value observed in suspended nanotubes [46] and suspended low density graphene [47], $\epsilon \approx 2$, incorporating short distance screening effects. The choice $\epsilon = 1$ would also appear to be natural [48], however, as we discuss later, this value seems to be inconsistent with the experimental observations of Ref. [25].

We also find that for these parameters, supported by the experimental data of Ref. [25], the Wigner crystal picture can be appropriate up to around $N \sim 26$ electrons, where the Wigner crystal starts to "melt". The crossover from the Wigner crystal to the electron liquid regime occurs at a crossover value $r_s \approx r^*_{1D}$, which we estimate based upon exact diagonalization calculations similar to those in Ref. [17] to be $r^*_{1D} \approx 3.3$ (see also Sec. V). At this crossover value of $r_s \approx r^*_{1D}$ (the boundary of the Wigner crystal regime) the one-dimensional density n^*_e of the electrons (holes) and their exchange coupling J^*

---

[3] An effective Heisenberg with inhomogeneous interaction has been used for trapped, strongly interacting one dimensional gases, see Refs. [64,65].

scale as

$$J^* \sim m^*/\epsilon^2, \quad n_e^* \sim m^*/\epsilon \ . \tag{4}$$

The effective mass of a semiconducting nanotube depends sensitively on the radius R of the nanotube, $m^* \sim 1/R$. Therefore the precise density range of Wigner crystal behavior as well as the energy scale of the exchange interaction in the Wigner crystal regime are very sensitive to the *radius* R of the tube as well as the precise *value of* ϵ. For a nanotube of radius $R = 3$ nm and $\epsilon = 4.5$, detailed estimates yielded a relatively small exchange coupling $J^* \approx 10$ K and a large crossover separation $d^* = 1/n_e^* = 50$ nm [27]. On the other hand, for a nanotube of radius $R = 1.6$ nm (yielding a band gap close to the one reported in Ref. [25]), and of moderate screening, $\epsilon \approx 2$, Eq. (4) immediately yields a surprisingly large "crossover" exchange coupling along with a small carrier separation,

$$J^* \sim 95 \text{ K}, \quad d^* \sim 11.8 \text{ nm}. \tag{5}$$

We thus conclude that the first transition line in Fig. 1 occurs well within the Wigner crystal regime, supporting the interpretation of the authors of Ref. [25], while the second transition line reaches into the melted region for high magnetic fields. We emphasize, however, that stronger screening by the environment, $\epsilon \gtrsim 4$ quickly reduces J^* to the few Kelvin range, a value close to the one observed in metallic nanotubes [49–51], and increases simultaneously the characteristic separation of particles to $d^* \sim 80$–100 nm.

The rest of the paper is structured as follows. In Sec. II, we determine the effective exchange interaction between two neighboring electrons in the Wigner crystal state and construct the effective spin Hamiltonian of a one dimensional electron crystal in the nanotube. In Sec. III, we analyze the magnetic excitations of small Wigner molecules and show how spin-orbit interaction breaks the SU(4) symmetrical spectrum to SU(2) × SU(2) multiplets. In Sec. IV, we investigate the spin structure of confined inhomogeneous nanotubes in an external magnetic field using a fermionic valence-bond calculation. Finally, before concluding, in Sec. V, we discuss the limitations and consistency of the Wigner crystal approach and present the simple scaling arguments, leading to the relations Eq. (4). Four appendices explain some useful details of these calculations.

II. CONSTRUCTION OF THE EFFECTIVE HAMILTONIAN

A. Derivation of the exchange coupling

To determine the exchange coupling in the Wigner crystal regime, we use a bottom-up approach. First, we model the interaction of two neighboring electrons in detail by semi-microscopic calculations [17], and extract their exchange interaction from the two-particle excitation spectrum. We find that the exchange interaction is quite accurately given by a semiclassical expression, similar to the ones used in Refs. [52,53].

In small diameter semiconducting nanotubes discussed here, and at scales larger than the atomic scale, the motion of the interacting N electrons (holes) is well described in terms of the lowest conduction (or highest valence) bands and the corresponding effective Hamiltonian

$$H = -\frac{\hbar^2}{2m^*}\sum_{i=1}^{N}\frac{\partial^2}{\partial z_i^2} + \sum_{i<j} U(z_{ij},\varphi_{ij}), \tag{6}$$

with z_i and φ_i denoting the particles' cylindrical coordinates (see also Appendix B).[4] The effective mass m^* here is simply related to the gap of the nanotube as $E_g = 2m^*c^2$ with $c \approx 8 \times 10^5$ m/s the Fermi velocity of graphene. For the sake of simplicity and concreteness, here we discuss electron-doped small radius semiconducting nanotubes, where the gap is mostly due to radial confinement and $E_g \approx 2\hbar c/3R$ [43], but our discussion carries over with trivial modifications to hole doping and nanotubes with strain or curvature induced gaps, too. In these latter cases, however, particles are typically lighter and it is harder to reach the Wigner crystal regime experimentally.

The Coulomb interaction

$$U(z,\varphi) = \frac{e^2}{\epsilon}\,\frac{1}{\sqrt{z^2 + 2R^2(1 - \cos\varphi)}}, \tag{7}$$

depends just on the distance between particles and thus $z \to z_i - z_j$ and $\varphi \to \varphi_i - \varphi_j$.[5] The dielectric constant ϵ depends crucially on the way the nanotube is prepared and contacted; for a nanotube laid over a typical semiconductor $\epsilon \sim 5$–7 seems to be a reasonable estimate [54], while in suspended nanotubes it may get close to the vacuum value, and $\epsilon \approx 2$–3 or possibly even smaller values seems to be a realistic choice [48,54].

Consider now two neighboring particles in the Wigner crystal regime, moving in the Hartree field of the other particles, and interacting with each other as described by the effective Hamiltonian

$$H^{(2)} = -\frac{\hbar^2}{2m^*}\left(\frac{\partial^2}{\partial z_1^2} + \frac{\partial^2}{\partial z_2^2}\right) + V(z_1) + V(z_2) + U(z_{12},\varphi_{12}). \tag{8}$$

The Hartree potential $V(z)$, displayed in Fig. 2, is well approximated in the Wigner crystal regime as

$$V(z) \approx \sum_{j\neq 1,2} U_0\big(z - z_j^{(0)}\big),$$

with the $z_j^{(0)}$ denoting the classically obtained locations of the other particles, and $U_0(z)$ the angular averaged Coulomb interaction,

$$U_0(z) \equiv \int_0^{2\pi}\frac{d\varphi}{2\pi}\,U(z,\varphi). \tag{9}$$

The angular dependence of the wave function is determined by the isospin (chirality) $\tau = \pm$ of the electrons,

---

[4] Notice that after projection to the lowest conduction band, the kinetic energy contains only the coordinates z_i, but the wave functions still have an angular dependence, as dictated by the chirality quantum number. The φ dependence therefore still appears in the interaction part of Eq. (6).

[5] A microscopic cutoff is usually also introduced to regularize it on the atomic scale (see Appendix B).

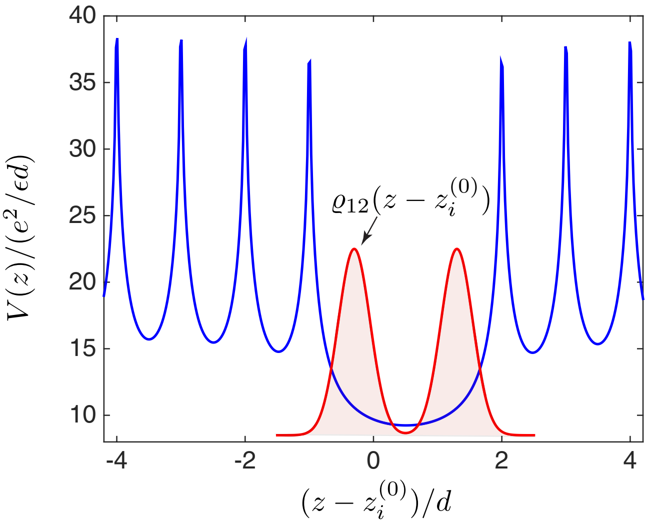

FIG. 2. Sketch of the effective potential, $V(z)$ (blue), and the single-particle density (red), as obtained from the solution of the two-body problem, Eq. (8). d is the distance between two neighboring electrons.

which also enters the two-particle wave function as $\psi = \Phi^{\sigma_1,\sigma_2}_{\tau_1,\tau_2}(z_1,z_2)\, e^{iQ(\tau_1\varphi_1+\tau_2\varphi_2)}$, with the angular momentum Q determined by the chirality of the tube[6] (details of the derivation are provided in Appendix A). The interaction term in Eq. (8) preserves the total isospin of the two interacting particles: $\tau_1 + \tau_2 = \tau_1' + \tau_2'$, but the matrix elements of $H^{(2)}$ do depend on the relative values of τ_1 and τ_1'. Nevertheless, while for $\tau_1 = \tau_1'$ integration over the angles yields the effective interaction, $U^{\tau_1\tau_2}_{\tau_1\tau_2}(z_{12}) = U_0(z_{12})$, the off-diagonal matrix elements of the potential, $U^{\tau_2\tau_1}_{\tau_1\tau_2}$ are found to be several orders of magnitude smaller than U_0 for $\tau_1 \neq \tau_2$ due to rapid oscillations of the wave functions [17]. Therefore, to a very good accuracy, the two-body Hamiltonian is diagonal in the spin and isospin quantum numbers, and the corresponding Schrödinger equation reads

$$E\,\Phi^{\sigma_1,\sigma_2}_{\tau_1,\tau_2} \approx \left[-\frac{\hbar^2}{2m^*}\left(\frac{\partial^2}{\partial z_1^2} + \frac{\partial^2}{\partial z_2^2}\right) + U_{\text{tot}}(z_1,z_2)\right]\Phi^{\sigma_1,\sigma_2}_{\tau_1,\tau_2} \tag{10}$$

with $U_{\text{tot}} = V(z_1) + V(z_2) + U_0(z_{12})$ the total two-body potential.

The chiral and spin quantum numbers are tied together with the orbital part of the wave function by Pauli's principle. Spatially, even solutions of (10) imply antisymmetry under exchanges $(\sigma_1,\tau_1) \leftrightarrow (\sigma_2,\tau_2)$, while odd solutions must be symmetric under them. Therefore the spectrum of the lowest 16 eigenstates of (10) is reproduced by the effective spin exchange Hamiltonian

$$H_J = \frac{J}{2}\, X^{\sigma}_{12} X^{\tau}_{12}, \tag{11}$$

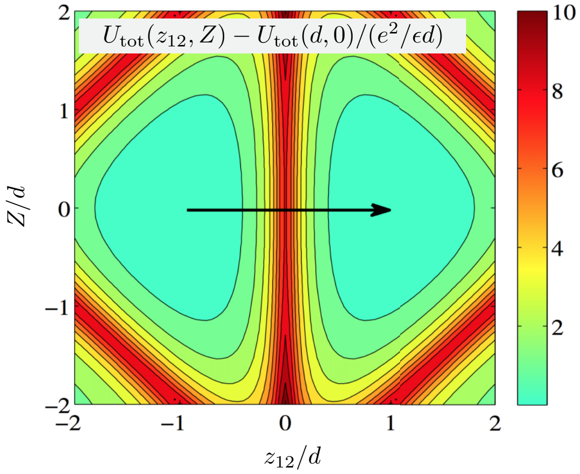

FIG. 3. Contour plot of the background potential U_{tot} in Eq. (10) in terms of relative and center of mass coordinates. Tunneling between the two minima ($z_{12} = \pm d, Z = 0$) gives rise to the exchange splitting J. The black arrow indicates the semiclassical tunneling path used here.

with J denoting the splitting of the sixfold degenerate ground state and the tenfold degenerate first excited multiplet. These large degeneracies are due to the (approximate) SU(4) symmetry of the exchange interaction.

The splitting J can be extracted by diagonalizing the two-body Hamiltonian [55] or, alternatively, in the Wigner crystal regime one can determine it with a remarkable ∼15% accuracy by means of a semiclassical approach (see Appendix C). Displaying the two-body potential U_{tot} in terms of the relative and center of mass coordinates z_{12} and $Z = (z_1 + z_2)/2$, we notice that the two particles move in a double-well potential (see Fig. 3). Tunneling processes along the tunneling path indicated in Fig. 3 lift the degeneracy of left and right states associated with the minima of U_{tot}, and give rise to the exchange splitting J.

The couplings J are displayed in Fig. 4 as a function of $n_e\, R$ for several experimentally relevant nanotube radii and $\epsilon = 2$. In these density units, the boundary of the Wigner crystal is at

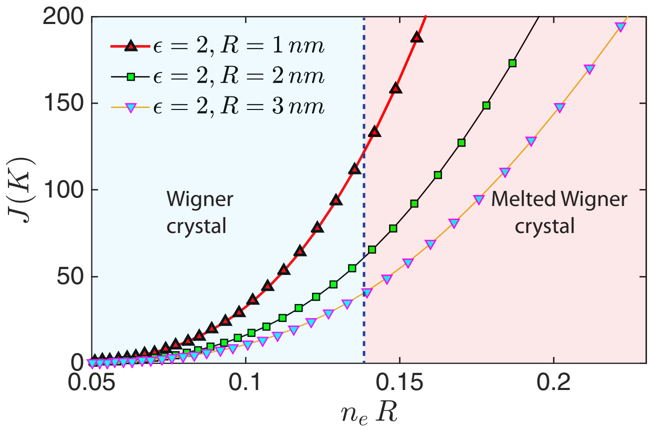

FIG. 4. The effective SU(4) spin-isospin exchange coupling J as a function of $n_e\, R$ for various nanotube radii with $\epsilon = 2$. The vertical dashed line shows the limit of the Wigner crystal regime.

---

[6] For a gapped zigzag nanotube of chirality $(3k + \nu, 0)$, considered here, $Q = 2k + \nu$ ($\nu = \pm 1$).

$(n_e R)^* \approx 0.135$ independently of the radius of the nanotube (see Sec. V). For small $R \approx 1$ nm radius nanotubes, we find that the exchange coupling can be as high as $J \sim 100$ K before the crystal starts to melt. This value can be even higher in case ϵ is closer to 1.

B. Effective spin Hamiltonian of a carbon nanotube Wigner crystal

Having determined the exchange coupling $J(n_e)$ in a homogeneous gas of electrons, we are now in a position to construct an effective Wigner crystal Hamiltonian. Assuming that the density of the electron or hole gas changes relatively slowly on the scale of typical particle-particle separations and that charges are pinned by some confining potential, we can neglect charge fluctuations and approximate the exchange coupling of two neighboring particles as $J(d)$, with $d = n_e^{-1}$ denoting their separation. We thereby arrive at the effective exchange Hamiltonian H_X in Eq. (2).

The spin-orbit coupling, Eq. (3), does not influence the exchange coupling substantially, and we have therefore neglected it in the previous section. However, deeper in the Wigner crystal regime (or in screened nanotubes) it can be comparable with J or larger, and can influence the spin state of the nanotube essentially [56]. The value of the coupling $\Delta_{\rm SO}$ is roughly inversely proportional to the radius of the tube, $\Delta_{\rm SO} R \sim 0.3$ meV nm, though sample to sample fluctuations can be large [43]. As already mentioned in Introduction, $H_{\rm SO}$ breaks the SU(4) symmetry of the exchange Hamiltonian (2) down to SU(2) × SU(2). However, $\Delta_{\rm SO}$ turns out to be relatively small in the crossover regime compared to the exchange coupling in poorly screened ($\epsilon \leqslant 2$) nanotubes. For a nanotube of radius $R = 1.6$ nm and $\epsilon = 2$, e.g., $\Delta_{\rm SO} \approx 2.1$ K [43], which is about a factor ~40 smaller than the exchange coupling in the crossover regime.

The symmetry of the Wigner crystal state is further reduced in the presence of an external magnetic field. Here we focus on the simple case of a magnetic field parallel to the axis of the nanotube, when

$$H_B = \sum_i \mu_B B\left(\frac{1}{2}\, g_s \sigma_i + g_{\rm orb} \tau_i\right) \qquad (12)$$

with $g_s \approx 2$ and $\mu_B = 0.057$ meV/T the Bohr magneton. Thereby the SU(2) × SU(2) symmetry of the crystal is further reduced to U(1) × U(1).

For an infinite nanotube the orbital g factor $g_{\rm orb}$ can be estimated as $g_{\rm orb} \approx 7\,R$ [nm], however, this value can be substantially reduced by confinement [40]. Therefore, for the nanotube in Fig. 1, we have used the experimentally extracted g factor, $g_{\rm orb} \approx 5.8$, corresponding to $\mu_{\rm orb} = g_{\rm orb}\,\mu_B \approx 0.33$ meV/T [25], yielding indeed good agreement for the phase boundaries in Fig. 1.

III. WIGNER MOLECULES

For small systems of $N = 2$ and 3 electrons (holes) Wigner molecules form, and we can diagonalize the effective Hamiltonians Eqs. (2) and (3) analytically to obtain their spin excitation spectrum. For $\Delta_{\rm SO} = 0$, the spectrum is organized into SU(4) multiplets characterized by Young tableaux. For a two-particle molecule, e.g., the lowest $4^2 = 16$ states are organized into a sixfold degenerate antisymmetric ground state multiplet and a tenfold degenerate symmetrical excited state (see Fig. 5).

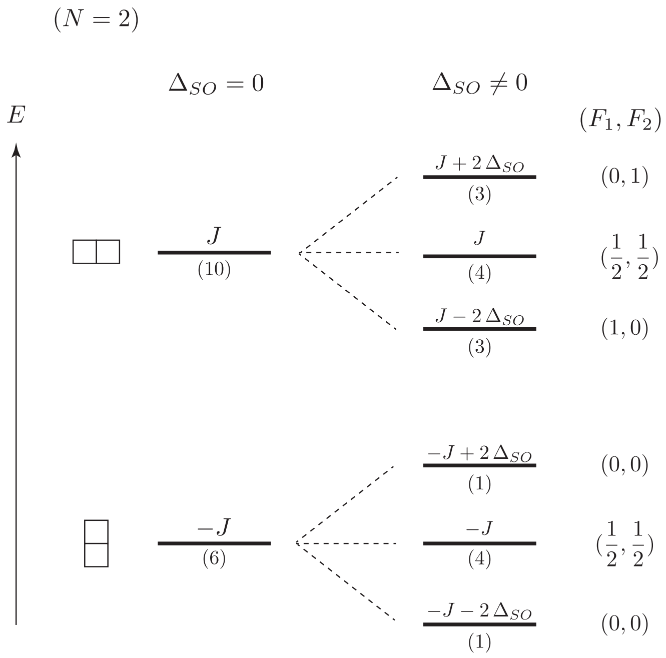

FIG. 5. Energy levels of an $N = 2$ Wigner molecule, as obtained from exact diagonalization of the effective Hamiltonian. On the left-hand side, the $\Delta_{\rm SO} = 0$ spectrum is shown, with states classified by SU(4) representations, indicated by the Young-tableaux. For $\Delta_{\rm SO} \neq 0$, states are classified in terms of the residual SU(2) × SU(2) symmetry.

These highly degenerate multiplets are split for $\Delta_{\rm SO} \neq 0$, and can be classified by the residual SU(2) × SU(2) symmetries, with their generators F_1 and F_2 inducing internal rotations within the τ_i, $\sigma_i = \pm 1$ subspaces. In terms of these latter, the sixfold degenerate ground state is split to two $(F_1,F_2) = (0,0)$ singlet states, and a fourfold degenerate $(F_1,F_2) = (1/2,1/2)$ excited multiplet. In contrast, the 10 times degenerate excited state splits into a fourfold degenerate $(F_1,F_2) = (1/2,1/2)$ multiplet, and two threefold degenerate multiplets, $(F_1,F_2) = (0,1)$ and a $(F_1,F_2) = (1,0)$ for $\Delta_{\rm SO} \neq 0$.

Injecting a third carrier into the nanotube, an $N = 3$-particle Wigner molecule forms. The Hilbert space of low-lying spin excitations is then 64-dimensional, these 64 states are, however, organized into just four SU(4) multiplets in the absence of $\Delta_{\rm SO}$: the fourfold degenerate ground state is again completely antisymmetric in the united spin-isospin space, while excited multiplets have mixed symmetries and are all 20-fold degenerate. Similar to the case of the $N = 2$ molecule, these states can be classified in terms of (F_1,F_2), too, and their spin-orbit coupling induced splitting and their energy can be exactly determined with group theoretical methods (see Fig. 6).

Injecting yet another carrier, an $N = 4$ Wigner molecule forms. In this case, even if we assume that the Wigner molecule is symmetrical relative to its center, two distinct couplings need to be introduced, one for the central bond (J), and another one

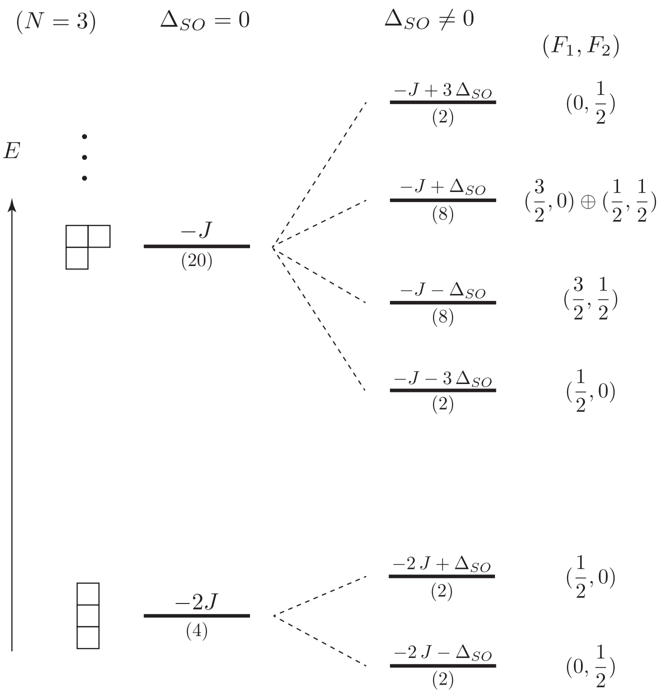

FIG. 6. Energy levels of a $N=3$ Wigner molecule. Only the first two SU(4) multiplets and their spin-orbit coupling induced splittings are shown.

for the two side bonds (J'). The excitation spectrum cannot be determined analytically in this case, but the ground state is found to be an SU(4) singlet, as expected. The approximately SU(4) symmetrical molecular states should be visible in the molecules' co-tunneling spectrum, and may lead to interesting quantum states when coupled to electrodes (see Summary and Conclusions) [57,58]. The SU(4) spin, coupled to two (SU(4)) Luttinger liquids, e.g., could give rise to an SU(4) two-channel Kondo state, characterized by an anomalous scaling dimension $\Delta=2/3$ [59]. Coupling the SU(4) Wigner molecule to side electrodes would, on the other hand, lead to an SU(4) Fermi liquid state.[7] The higher-dimensional SU(4) spins may give rise to exotic underscreened Kondo states.

IV. WIGNER CRYSTAL STATE IN A PARABOLICALLY CONFINED NANOTUBE

We now turn to the experimental setup of Ref. [25], where the nanotube was attached to source, drain, and gate electrodes. In this case, the attached gate electrodes can produce Schottky barriers at the ends of the nanotube, and charges accumulated there are expected to create a smooth external, approximately parabolic confinement potential for the charge carriers:

$$V_{\mathrm{conf}}\approx \tfrac{1}{2}\alpha\,z^2. \qquad (13)$$

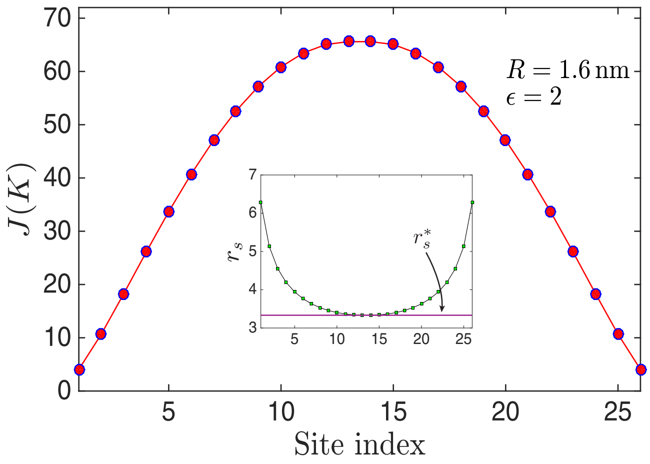

FIG. 7. Site dependent exchange couplings for a nanotube with $\epsilon=2$ and $R=1.6$ nm when $N=26$ electrons are confined inside. The inset shows the dimensionless parameter r_s as a function of the site index. Notice that the stability condition $r_s \gtrsim r_s^*\simeq 3.3$ is fulfilled, and the nanotube is in the Wigner crystal regime, though for larger values of N the Wigner crystal is expected to melt at the center of the nanotube.

The depth of the potential, $\alpha=m^*\omega_0^2$ can be estimated from the measured charging energy of the nanotube (see Appendix D for details). Throughout the present work we consider $\alpha\approx 0.015\ \mathrm{meV/nm^2}$, which for $\epsilon=2$ corresponds to a charging energy of $U\approx 15$ meV, in rough agreement with the value reported in Ref. [25], $U\approx 10$–12 meV. For a $R=1.6\,\mathrm{nm}$ nanotube this corresponds to a confinement energy $\hbar\,\omega_0\approx 6.25$ meV.

In a parabolic confinement, the gas of particles is denser at the central region of the tube, and correspondingly, the exchange coupling J_i is larger there, and decreases towards the ends of the tube. In the experiments, the gate voltage is varied, and the number of the charge carrier increases one by one until the Wigner crystal gradually melts at the center of the tube. For each N, we therefore need to determine the dynamical rearrangement of the particles and, accordingly, a new distribution of the couplings J_i. To this end, we minimized the classical Coulomb energy of the particles in the confining potential,

$$E=\sum_{i=1}^{N}\frac{m^*\omega_0^2}{2}z_i^2+\sum_{i<j}^{N}\frac{e^2}{\epsilon|z_i-z_j|}\,.$$

Figure 7 shows the spatial dependence of the inhomogeneous couplings and the position dependent interaction parameter r_s for $N=26$ charged particles in a nanotube of $\epsilon=2$ and $R=1.6$nm. Remarkably, r_s remains above the crossover value $r_s^*\approx 3.3$ even at the center of the tube, where the exchange coupling is as large as $J\sim 65$ K, and the whole nanotube is in the Wigner crystal regime. For larger values, $N>26$, however, r_s becomes smaller that r_s^* at the center of the nanotube, and the core of the Wigner crystal melts.

To determine the spin state of the relaxed Wigner crystal, we performed a valence bond mean field calculation. We first grouped the spin and isospin variables as $(\sigma,\tau)\to a$, and rewrote the exchange interaction in a readily SU(4) invariant

---

[7] The exponent Δ refers to the case of the SU(4) × SU(2) model with Fermi liquid leads. This exponent is, however, expected to remain unchanged in the Luttinger liquid case, too, since correlators (i.e., spin excitations) in the SU(4) spin sector of the leads are expected to remain unaffected by the Luttinger parameter K of the charge sector.

form as

$$H_X = \sum_i \sum_{ab} \frac{J_i}{2}\, c^\dagger_{i\,a} c_{i\,b} c^\dagger_{i+1\,b} c_{i+1\,a} \equiv \sum_i \sum_{ab} \frac{J_i}{2}\, S_i^{a\,b} S_{i+1}^{b\,a}, \tag{14}$$

with the fermionic operators $c^\dagger_{i\,a}$ $(c_{i\,a})$ creating (annihilating) a carrier on site i, and satisfying the constraint $\sum_a c^\dagger_{i\,a} c_{i\,a} = 1$ at each site. The operators $S_i^{a\,b} = c^\dagger_{i\,a} c_{i\,b}$ obey the SU(N) commutation relations $[S_i^{a\,b}, S_j^{a'\,b'}] = \delta_{i,j}(\delta_{a\,a'} S_i^{b\,b'} - \delta_{a\,b'} S_i^{a'\,b})$. The terms H_{SO} and H_B can also be expressed in terms of the SU(4) spin operators, $S_i^{a\,b}$, and obviously break the SU(4) symmetry of H_X. Notice that the Hamiltonian (14) is also invariant under local gauge transformations, $c_{j\,a} \to c_{j\,a} e^{i\theta_j}$, reflecting local particle number conservation.

In the presence of the terms H_{SO} and H_B, the inhomogeneity in the exchange coupling plays a crucial role. For longer Wigner chains, the exchange coupling J_i is very strong at the center of the chain, while at the wings it can be smaller by two or more orders of magnitude. Therefore, in the presence of an external magnetic field, the nanotube may be phase separated, with wings polarized in isospin and spin space, and the center of the chain remaining in an approximately SU(4) antiferromagnetic Néel state. For smaller external magnetic fields, all three phases can be present in the nanotube: a spin-isospin polarized state at the wings, where the field-induced Zeeman and orbital splitting are much larger than the exchange coupling, an antiferrmagnetic state at the center, where the exchange coupling dominates over the magnetic field, and an orbitally polarized spin antiferromagnet between them.

This competition of H_{SO} and H_B leads to the nontrivial phase diagram shown in Fig. 1, constructed in Ref. [25] by investigating the change in total magnetization while adding an extra particle in a magnetic field, $\Delta M(N) = M(N+1) - M(N)$, a quantity which can be directly extracted through transport measurements from the shift of the Coulomb blockade peaks in a magnetic field. To understand this phase diagram, we must keep in mind that the Wigner crystal is inhomogeneous and therefore the density and the exchange coupling are both the largest at the center of the nanotube. Consider now adding particles to the nanotube in a fixed external magnetic field. For small particle numbers, the exchange coupling remains small even at the center of the nanotube, and both the spins and the isospins of the entering particles are found to be completely polarized (phase I). For increasing particle numbers, however, the density and thus the exchange coupling at the center start to become larger, and the latter exceeds the spin splitting of the SU(4) spins, induced by the external magnetic field, but remains still smaller than the orbital splitting, due to the difference in the electronic and orbital g factors. As a consequence, new particles enter with alternating spins but polarized isospin (isospin polarized spin antiferromagnet, phase II). Finally, for even larger particle numbers, the exchange coupling at the center of the tube dominates, and electrons enter with alternating spin and orbital spins (spin-isospin antiferromagnet, phase III). Notice that the three regions in Fig. 1 are not true phases. In region II, e.g., the nanotube hosts two magnetic phases: an orbitally polarized spin antiferromagnet at the center, and regions of fully polarized spins and isospins on the wings.

To analyze the spin-isospin configurations of the confined Wigner crystal theoretically, we made use of a self-consistent valence bond approach, whereby we decouple the exchange term assuming a finite $Q_i = \langle \sum_a c^\dagger_{i+1\,a} c_{i\,a} \rangle$ to obtain

$$H_{\mathrm{MF}} = -\sum_{i\,a} J_i\,(Q_i \cdot c^\dagger_{i+1\,a} c_{i\,a} + \mathrm{H.c.}) + \sum_{i\,a} \mu_i \cdot c^\dagger_{i\,a} c_{i\,a} + H_{\mathrm{SO}} + H_{\mathrm{B}}. \tag{15}$$

Here the Lagrange multipliers μ_i ensure that particle number is conserved on the average at each site and, similar to the Q_i, must be determined self-consistently [60]. Notice that, by the local gauge invariance of (14), the Q_i are not uniquely defined, and the energies of the ground states of H_{MF} remain invariant under the transformation $Q_i \to Q_i e^{i(\theta_i - \theta_{i+1})}$. This simple mean-field approach captures surprisingly well the properties of SU(4) and SU(2) antiferromagnets and, according to our findings, can also account for the phase diagram of the carbon nanotube Wigner crystal.

The phase diagram represented in Fig. 1 has been determined by performing self-consistent calculations for each magnetic field and for up to $N = 35$ particles. As already stated in Introduction, apart from ϵ, which we have set to $\epsilon = 2$ to agree with the values reported so far in suspended graphene and nanotubes [47,54], all parameters have been estimated from the experiments: The parameter α can be estimated from the charging energy $U \sim 10$–12 meV, and is found to be in the range $\alpha \approx 0.005$–$0.015\ \mathrm{meV/nm^2}$ (see Appendix D). Here we shall use the value $\alpha = 0.015\ \mathrm{meV/nm^2}$ yielding the closest resemblance to the experimental data of Ref. [25]. The radius $R = 1.6$ nm is determined from the curvature-induced gap $E_g \approx 220$ meV reported in Ref. [25] (and is directly related tho the effective mass, $E_g \approx 2m^* c^2$), and yields a spin-orbit splitting $\Delta_{\mathrm{SO}} \approx 2.1$ K (see Ref. [43]). Finally, we have used the experimentally measured value, $g_{\mathrm{orb}} \approx 5.8$ [25].

Results of these simulations have been summarized in Fig. 1. Though the magnetization pattern may be not as systematic as the ones reported in Ref. [25]—possibly due to our approximate valence bond method—the similarity and the correct location of the phase boundaries are, nevertheless, striking. The overall good agreement is, however, shaded by the fact that for these parameters the density of the electron crystal starts to exceed the crossover value n_e^* for $N \gtrsim 26$ at the center (see Appendix D). A somewhat weaker confinement, $\alpha \approx 0.01\ \mathrm{meV/nm^2}$ increases this characteristic value of N, and yields also a charging energy in better agreement with the experimentally observed value, but the agreement of the phase diagram in Fig. 1 gets worse.

V. RANGE OF VALIDITY OF THE WIGNER CRYSTAL DESCRIPTION AND SCALING RELATIONS

Throughout our previous analysis, we assumed that electrons are reasonably localized by their strong Coulomb interaction. While this assumption is certainly not correct for an infinite chain, where charge fluctuations are unlimited and no long-ranged charge order exists even at $T = 0$ temperature, it can certainly be applied in a finite system, where charge fluctuations are pinned. Then our approach is valid under the condition that typical quantum fluctuations of the localized charges be less than their separation, $\Delta z \ll d$.

The ratio $\Delta z/d$ is directly related to the parameter r_s. Computing the width of a Gaussian wave function self-consistently within the Coulomb potential of an infinite chain of particles yields the simple estimate (see Appendix B)

$$\frac{\Delta z}{d} = \left(\frac{1}{4\,F\,r_s}\right)^{1/4} \tag{16}$$

with the geometrical factor F depending on the densities (wave functions) of the other localized charges. For perfectly localized particles, we find $F = \zeta(3) \approx 1.202$, with ζ the Zeta function (see Appendix B). However, the factor F increases as one approaches the border of the Wigner crystal regime, $r_s \approx r_{1D}^*$, which we define as the value of r_s, where the charge density is suppressed by a factor of 2 as one moves from one lattice position to the next one, a condition yielding $d/\Delta z \approx 2.35$ for Gaussian wave packets. Smearing the electron charges then in boxes of width $2\,\Delta z$ yields $F \approx 1.70$ at the transition, corresponding to the rough estimate, $r_s \approx r_{1D}^* \approx 4.4$.

A more accurate way to estimate r_{1D}^* is to perform calculations for a molecule in a harmonic trap, where one can squeeze the atoms together by increasing the confinement frequency ω_0 [17]. The crossover density and thus r_{1D}^* can then be determined by just looking at the separation d of the two charges when the charge density at the center is reduced by a factor of 2. This more accurate procedure yields the crossover value $r_{1D}^* \approx 3.3$, used throughout this paper.

Now we show that at the crossover, $r_s = r_{1D}^*$, the exchange coupling J^* and the density n_e^* obey the scaling relations, Eq. (4). To prove this, we first observe that, according to our discussion in Sec. II A, the electron-electron interaction can be replaced by the angular averaged interaction, $U_0(z,R)$ in Eq. (9). Introducing the dimensionless coordinates, $\xi_i \equiv n_e z_i$, the Hamiltonian of the interacting particles becomes

$$H = \frac{\hbar^2 n_e^2}{m^*}\,\mathcal{H}, \tag{17}$$

with the dimensionless Hamiltonian $\mathcal{H} = \mathcal{H}(r_s,n_e R)$ given by

$$\mathcal{H} = \sum_i -\frac{1}{2}\frac{\partial^2}{\partial \xi_i^2} + r_s \sum_{i<j} u_0(\xi_{ij}, R\,n_e), \tag{18}$$

where the dimensionless averaged Coulomb interaction u_0 trivially depends on the dimensionless parameter $n_e R$. Thus, in the dilute limit $n_e R \ll 1$, we have $\mathcal{H} \approx \mathcal{H}(r_s,0)$, and the structure of the dimensionless wave function and the energy spectrum of the dimensionless Hamiltonian $\mathcal{H}$ depend only on r_s. It follows immediately that at the crossover point, $r_s = r_{1D}^* \approx 3.3$, the density of the gas scales as

$$n_e^* = \frac{1}{r_{1D}^*}\frac{e^2 m^*}{\epsilon\,\hbar^2} \sim \frac{m^*}{\epsilon}, \tag{19}$$

while the exchange energy is just a universal number (A) apart from the overall energy scale in Eq. (17),

$$J^* = A\,\frac{\hbar^2 n_e^{*2}}{m^*} \sim \frac{m^*}{\epsilon^2}. \tag{20}$$

Equation (20) just follows from the fact that, in the spirit of the virial theorem—at the crossover, the Coulomb, the kinetic, and the exchange energies are all approximately equal, while Eq. (19) states that the density of the gas is inversely proportional to the effective Bohr radius.

These general scaling relations hold under the condition $n_e^* R \ll 1$. Using the relation $m^* = \hbar^2/(3R\gamma)$ [43] with $\gamma = 0.54$ eV nm (yielding, e.g., $m^* \simeq 0.0294\,m_e$ for a nanotube of radius $R = 1.6$ nm), this condition simplifies to

$$n_e^* R \approx \frac{0.27}{\epsilon} \ll 1. \tag{21}$$

This inequality is well satisfied for even slightly screened nanotubes with $\epsilon \sim 2$–3, but we find that relations (4) are also obeyed by the exchange couplings and densities extracted from the two-body spectrum of unscreened nanotubes with $\epsilon = 1$, for which (21) is certainly only poorly satisfied.

VI. SUMMARY AND CONCLUSIONS

In this work, we attempted to account for the magnetic behavior of a Wigner crystal that forms in a confined semiconducting carbon nanotube. We have carefully estimated the exchange interaction (J) between neighboring localized electrons (holes) in the crystalline state, and have shown that it is SU(4) symmetric with very good accuracy. For poorly screened small diameter semiconducting nanotubes, the semimicroscopically determined exchange couplings at the melting of the crystal turn out to be surprisingly large, $J^* \sim 100$ K. These large values follow from very robust scaling arguments, and are also in agreement with experiments [25,27] as well as independent theoretical computations [17,27], also reproduced here. As we argued, at the crossover the exchange coupling J^* is just proportional to the effective Bohr energy, with m_e replaced by m^* and with an additional factor $1/\epsilon^2$, yielding the simple estimate, $J^* \sim m^*/(m_e\epsilon^2) \times 1$ Ry. Determining the numeric prefactor omitted here requires more accurate computations, but it is not unreasonable to assume it is in the range of 0.01–0.1. For a nanotube with $R \approx 1.6$ nm and $\epsilon = 2$, this heuristic estimate gives 10 K to 100 K, consistent with our more accurate calculations.

Spin-orbit coupling (Δ_{SO}) breaks the SU(4) spin symmetry down to SU(2) × SU(2) [61]. As we demonstrated in Sec. III, for small, $N = 2 - 4$ particle Wigner molecules, the interplay between J and Δ_{SO} leads to interesting spin excitation spectra with excited states classified as SU(2) × SU(2) multiplets. This intriguing spin spectrum should readily be seen in the co-tunneling spectrum of Wigner molecules, would provide direct information on J, Δ_{SO}, and would also evidence the underlying SU(4) and the residual SU(2) × SU(2) symmetries.

The interesting spin structure of the molecule can lead to exciting quantum states when the molecule is coupled to electrodes [57,58]. For small Δ_{SO}, the SU(4) spin, coupled to two (SU(4)) Luttinger liquids, e.g., may give rise to a SU(4) two-channel Kondo state, characterized by an anomalous scaling dimension $\Delta = 2/3$ [59]. Coupling the SU(4) Wigner molecule to side electrodes would, on the other hand, lead to an SU(4) Fermi liquid state, while higher-dimensional SU(4) spins may give rise to exotic underscreened Kondo states. A finite Δ_{SO} will, however, induce a crossover to SU(2) × SU(2) states, and lead to less exciting SU(2) Kondo physics at low temperatures.

We remark that the competition between J and Δ_{SO} has even more exciting implications for homogeneous crystals [56]. The spin-orbit coupling breaks the original SU(4) spinon excitations of the SU(4) antiferromagnet into SU(2) spinons propagating with 3 different spin velocities, and leads to a quantum phase transition with one of the spinons becoming gapped as we move deeper into the Wigner crystal regime.

To test our bottom-up approach, we have performed a detailed modeling of the experiments of Ref. [25]. We estimated the basic model parameters (m^*, g_{orb}, and confinement strength α) directly from the experiments. We have set the unknown dielectric constant to $\epsilon = 2$ [54]. Performing a self-consistent valence-bond calculation for an increasing number of electrons in an external magnetic field, we recovered the experimentally observed magnetic phase boundaries with reasonable accuracy. As we have discussed in Sec. IV, these phase boundaries from the inhomogeneity of the crystal, and do not correspond to new phases, rather they can be interpreted as the emergence of different types of antiferromagnetic domains at the center of the nanotube, where the density and thus the exchange coupling are both the largest. Given the simple multiscale calculations we performed, the good agreement with the experiments is striking.

We should remark though that while the phase boundaries we get are qualitatively and quantitatively very close to the experimentally observed ones, we do not observe regular twofold magnetization patterns, our patterns are closer to the ones presented in the supplemental information of Ref. [25]. This may be a consequence of the valence-bond approach we employed or possibly the melting of the Wigner crystal for larger particle numbers, which for our parameters occurs at $N \gtrsim 26$.

We should also comment here on the value of the dielectric constant ϵ. It would be natural to assume that $\epsilon \approx 1$ in a nanotube suspended in vacuum [47,48,54]. However, such a small value of ϵ is inconsistent with the data. For $\epsilon = 1$, only a shallow parabolic confinement with $\alpha \lesssim 0.003\ \mathrm{meV\,nm^{-2}}$ can yield charging energies compatible with the experimentally reported values, $U \sim 10$ meV (see Appendix D). For such shallow confinement, the unscreened Coulomb repulsion pushes the charges quickly towards the end of the nanotube, and already for about $N \sim 10$ they form a homogeneous crystal all over the nanotube. Such a homogeneous crystal is clearly incompatible with the experiments: in such a crystal, exchange couplings are approximately equal, and a huge magnetization jump should occur at a critical magnetic field, $B \sim J/\mu_{\mathrm{orb}}$, not seen experimentally. Furthermore, such a homogeneous Wigner crystal will not melt gradually, but would develop a sudden transition in the whole crystal once the melting condition $r_s \lesssim r^*_{1D}$ is satisfied.

Thus the value $\epsilon \approx 1$ seems to be incompatible with the experimental data. So are larger values of $\epsilon \gtrsim 4$. For these large values, a very large confinement would be needed to yield $U \sim 10$ meV. By our scaling arguments, the exchange coupling should then be less than $J^* \sim 10$ K, clearly inconsistent with the high field phase boundary observed in Ref. [25] and the corresponding exchange coupling, $J \sim 60$ K. Furthermore, in this case the crystal would melt very quickly, once a few particles enter the tube.

We thus conclude that only $\epsilon \approx 2$ seems to give a consistent explanation for the data reported in Ref. [25]. For this value of ϵ the first transition between the completely polarized state and the spin-antiferromagnet (see Fig. 1) occurs well in the Wigner crystal regime, however, for $N \sim 26$, the Wigner crystal should melt, and our approach becomes questionable. The description of this regime of a partially melted confined Wigner crystal and the crossover between the Wigner crystal and electron (Luttinger) liquid regimes is a true theoretical challenge.

While spin-orbit coupling gives rise to interesting spin excitations in small molecules, we find that for a semiconducting nanotube of radius $R = 1.6$ nm, corresponding to the gap measured in Ref. [25], Δ_{SO}, does not have a large impact on the magnetic states within the phase diagram. It eliminates the orbitally polarized phase at very small fields but, apart from that, the phase diagram remains almost identical to that of an SU(4) symmetrical Wigner crystal with $\Delta_{\mathrm{SO}} \to 0$.

Let us finally comment on the general implications of our results and their limitations. Although we focused on semiconducting (zigzag) nanotubes, most of our considerations are very general, and also apply with trivial modifications to metallic tubes with curvature or strain induced band gaps and semiconducting nanotubes of other chirality. In particular, the scaling relations (4) are very general, and imply that the range of applicability of the Wigner crystal picture as well as the strength of the exchange coupling depend extremely sensitively on the parameters of the tube and details of the experimental setup; to observe the Wigner crystal and its magnetic structure it is essential to avoid strong screening and to increase the effective mass of the particles as much as possible. In practical terms, small radius or strongly strained suspended nanotubes of $\epsilon \lesssim 2$ are best to observe the detailed structure of the crystal. Correspondingly, while the nanotube studied in Ref. [25], is found to be in the Wigner crystal regime for electron numbers $N \lesssim 26$, metallic nanotubes with small strain-induced gap laid on or close to a substrate are extremely unlikely to host Wigner molecules, and should rather be described in terms of extended electron (hole) states.

ACKNOWLEDGMENTS

We would like to thank Shahal Ilani, Christoph Strunk, Milena Grifoni, and especially to András Pályi for important and fruitful discussions, and to Răzvan Chirla for the careful reading of the manuscript. This work has been supported by the Hungarian research grant OTKA K105149, by NSF DMR Grant No. 1603243 (LG) and by UEFISCDI Romanian Grant No. PN-II-RU-TE-2014-4-0432 (CPM).

APPENDIX A: CONSTRUCTION OF LOCALIZED SINGLE-PARTICLE STATES IN A ZIGZAG CARBON NANOTUBE

In this appendix, we construct the wave function of the localized electrons forming the Wigner crystal. The Brillouin zone (BZ) of the underlying graphene sheet is represented in Fig. 8, with the two inequivalent Dirac points denoted as K and K'. Rolling up the graphene into a carbon nanotube (CN) restricts the BZ to some parallel line segments [62], with their orientation dictated by the chirality of rolling the nanotube.

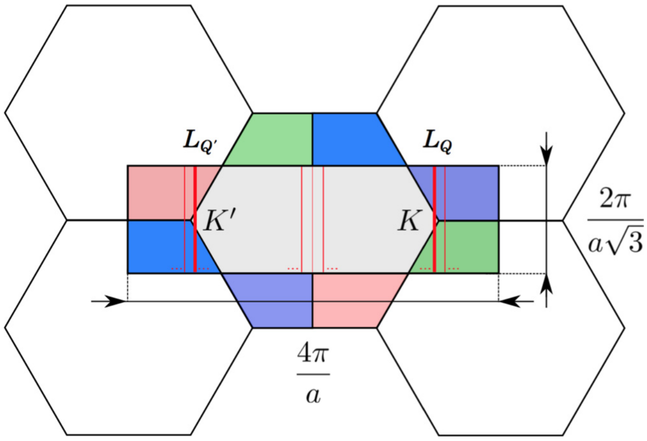

FIG. 8. Retailored Brillouin zone (BZ) of graphene (black rectangle). The red lines denote states allowed for a zigzag carbon nanotube, K and K' mark the two Dirac points, a is the lattice constant. Thick solid red lines indicate the segments $L_{\pm Q}$.

Here, for simplicity, we consider semiconducting zigzag CN's with chirality $(n,0)$ and radius $R = a\,n/2\pi$ $(n = 3k + \nu;\ \nu = \pm 1)$. In this case, allowed states in the graphene BZ consist of segments of length $2\pi/a\sqrt{3}$ parallel to the k_z direction (vertical red lines in Fig. 8), and the lowest lying excitations are on the segments closest to $\mathbf{K} = -\mathbf{K}' = (4\pi/3a,0)$. The minimum-energy point of these vertical segments is at the points $\mathbf{Q} = -\mathbf{Q}' = (Q,0)$ with $Q = (2n + \nu)/(3R)$. For low-density CNs, it is enough to restrict ourself to these two segments, $L_{\pm Q} = (\pm Q, q_z)$, indexed by the isospin quantum numbers $\tau = \pm 1$. Along these lines, for small q_z, excitations are massive Dirac fermions with a dispersion

$$\varepsilon_\tau(q_z) \approx \pm\sqrt{c^2 q_z^2 + (m^*)^2 c^4}, \tag{A1}$$

with $c \approx 8 \times 10^5$ m/s the Fermi velocity of graphene and m^* the effective mass

$$m^* = \frac{\hbar}{3Rc}\,. \tag{A2}$$

The wave functions (of the unrolled nanotube) for the electrons (holes) can be expressed by Bloch's theorem as $\psi^\pm_{\mathbf{k}}(\mathbf{r},\zeta) = \mathrm{e}^{\mathrm{i}\mathbf{kr}}\, u^\pm_{\mathbf{k}}(\mathbf{r},\zeta)$. Here we explicitly separate the position vector into a two dimensional vector within the graphene sheet, $\mathbf{r}$, and a coordinate ζ perpendicular to it. In cylindrical coordinates of the nanotube $\mathbf{r} = (R\varphi, z)$, and the wave functions along the line segment $\mathbf{k} \in L_{\tau Q}$ read

$$\psi^\pm_{\mathbf{k}} = e^{\mathrm{i}Q\tau\varphi}\, e^{\mathrm{i}q_z z}\, u^\pm_{\mathbf{k}}(R\varphi, z, \zeta) \tag{A3}$$

with $r = R + \zeta$. These wave functions describe particles of chirality τ circulating around the tube.

In the Wigner crystal, we create wave packets from the states (A3)

$$\Psi^\pm_{j\tau}(\mathbf{r},\zeta) = \int_{\mathbf{k}\in L_{\tau Q}} dq_z\; e^{\mathrm{i}\mathbf{kr}} \cdot u^\pm_{\mathbf{k}}(\mathbf{r},\zeta) \cdot f(q_z), \tag{A4}$$

with $f(q_z) \propto \mathrm{e}^{-\mathrm{i}\bar{z}q_z}\mathrm{e}^{-\frac{1}{2}\Delta z^2 q_z^2}$ a Gaussian envelope, and $\bar{z}$ the location of the wave packet along the nanotube. Assuming that $u^\pm_{\mathbf{k}}$ only weakly depends on $\mathbf{k}$, we obtain the quasiparticle wave function at position $\bar{z} = z_j^{(0)}$,

$$\Psi^\pm_{j\tau\sigma} = \frac{1}{\sqrt{2\pi}}\, e^{\mathrm{i}\,Q\tau\varphi}\, \frac{1}{(\pi\ \Delta z)^{1/4}}\, e^{-\frac{(z-z_j^{(0)})^2}{2\,\Delta z^2}}\ \chi_\sigma\ u^\pm_{\tau\mathbf{Q}}(z,\varphi,\zeta), \tag{A5}$$

with the $\pm$ sign referring to electrons and holes, and χ_σ representing the spin part of the wave function. The Bloch functions $u_{\pm\mathbf{Q}}(\mathbf{r},\zeta)$ in (A4) describe an almost homogenius background charge pattern, which varies only at the atomic scale, and can be ignored in many cases. We should emphasize that the single band approach presented here is only be valid for wide enough wave packets,

$$\Delta z > \sqrt{3}R. \tag{A6}$$

APPENDIX B: THE EFFECTIVE COULOMB POTENTIAL

The Coulomb potential in cylindrical coordinates is

$$U(z,\varphi) = \frac{e^2}{\epsilon}\,\frac{1}{\sqrt{z^2 + \bar{\alpha}^2 + 2R^2(1 - \cos\,\varphi)}} \tag{B1}$$

with e the electron charge and ϵ the relative dielectric constant. In the exact diagonalization approach of Ref. [17] the microscopic cutoff $\bar{\alpha}$ describes a crossover between the Coulomb potential and a Hubbard-like short range interaction for $z \to 0$, and was fixed to $\bar{\alpha} = e^2/U_0\,\epsilon$, with $U_0 = 15$ eV. Then, the average interaction felt by two electrons at a distance z is

$$\begin{aligned} U_0(z) &= \int_0^{2\pi} \frac{d\varphi}{2\pi}\, U(z,\varphi). \\ &= \frac{e^2}{\epsilon}\,\frac{1}{|z|}\, f(z/R, \bar{\alpha}/R) \end{aligned} \tag{B2}$$

with $f(z/R,\bar{\alpha}/R)$ a dimensionless function

$$f\left(\frac{z}{R},\frac{\bar{\alpha}}{R}\right) = \frac{|z|}{\sqrt{z^2 + \bar{\alpha}^2 + 4R^2}}\, K\left(\frac{2R}{\sqrt{z^2 + \bar{\alpha}^2 + 4R^2}}\right) \tag{B3}$$

given in terms of the complete elliptic integral of the first kind, $K(x)$ [63]. The screening length $\bar{\alpha}$ in Eq. (B3) is of the order $\bar{\alpha} \sim 0.1$ nm$/\epsilon$, is much smaller than R, and regularizes the potential in the limit $z \to 0$, while for large distances, $z \gg R$ the usual Coulomb behavior is recovered,

$$U_0(z \gg R) \approx \frac{e^2}{\epsilon}\,\frac{1}{|z|}. \tag{B4}$$

The Hartree potential felt by particle i is given by $V_i^{(1)}(z) = V^{(1)}(z - z_i^{(0)})$ with

$$V^{(1)}(z) = \sum_{j\neq 0} \int dz' \frac{d\varphi'}{2\pi}\frac{d\varphi}{2\pi}\, U(z - z', \varphi - \varphi')|\Psi_{j\tau\sigma}(z',\varphi',\zeta)|^2. \tag{B5}$$

Deep in the Wigner crystal the wave functions are well localized, and to a good approximation

$$V^{(1)}(z) \approx \sum_{j\neq 0} U_0\big(z - z_j^{(0)}\big), \tag{B6}$$

with $U_0(z)$ given by Eq. (B2). The resulting Hartree potential is shown in Fig. 9. A similar procedure yields the two-particle potential displayed in Fig. 2.

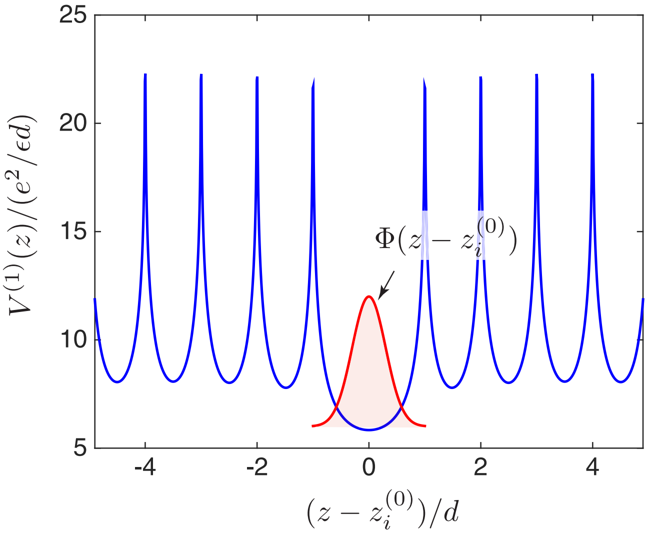

FIG. 9. The Hartree potential $V_i^{(1)}(z)$ confining the ith electron, defined in Eq. (B6).

We now estimate the extension of the wave function in this Hartree potential. We first approximate $U_0(z - z_j^{(0)})$ by a Coulomb potential to obtain the following parabolic approximation by expanding (B6):

$$V^{(1)}(z) \approx V^{(1)}(0) + \frac{2e^2}{\epsilon\, d^3}\zeta(3)\, z^2,$$

with $d = n_e^{-1}$ the separation of electrons and $\zeta(3) = \sum_{k=1}^{\infty} 1/k^3 \approx 1.202$.[8] Solving the harmonic oscillator problem in this harmonic potential yields then a simple estimate, Eq. (16).

APPENDIX C: EXCHANGE INTERACTION IN A WIGNER MOLECULE

In this appendix, we present the semiclassical approach to determine the exchange interaction J, which we also compare with the results of exact diagonalization [17,27]. We consider two interacting electrons of mass m^* in a parabolic confining potential of frequency ω_0. The Schrödinger equation can be factorized in this case in terms of the relative ($z = z_2 - z_1$) and center of mass [$Z = (z_1 + z_2)/2$] coordinates, $H = H_{\text{rel}}(z) + H_{\text{COM}}(Z)$. The center of mass motion is that of a harmonic oscillator of frequency ω_0, and is completely decoupled from the relative motion described by the single-particle Hamiltonian,

$$H = -\frac{\hbar^2}{2\mu}\frac{\partial^2}{\partial z^2} + \frac{1}{2}\,\mu\,\omega_0^2 z^2 + \frac{e^2}{\epsilon}\frac{1}{|z|} f\left(\frac{z}{R},\frac{\alpha}{R}\right), \tag{C1}$$

with $\mu = m^*/2$ the reduced mass and $f(z/R,\bar{\alpha}/R)$ the cutoff function in Eq. (B3). With a good accuracy, we can set the parameter $\bar{\alpha}/R$ to zero. We can then make the Hamiltonian dimensionless by introducing the dimensionless coordinate, $\rho = z/\lambda$, with $\lambda = (\hbar/m^*\omega_0)^{1/2}$ the noninteracting oscillator length, and dividing it by the natural energy scale, $\hbar\omega_0$. In these units, the Hamiltonian becomes

$$\mathcal{H} = \mathcal{T} + \mathcal{V}(\rho) = -\frac{\partial^2}{\partial \rho^2} + \frac{1}{4}\rho^2 + \tilde{r}_s\frac{1}{|\rho|} f\left(\rho\,\frac{\lambda}{R}\right), \tag{C2}$$

with $\tilde{r}_s$ characterizing the strength of Coulomb interaction compared to that of the parabolic confinement,

$$\tilde{r}_s = \frac{e^2}{\hbar\omega_0\,\epsilon\lambda}. \tag{C3}$$

Notice that $\tilde{r}_s$ in Eq. (C3) is different from the usual r_s, defined by Eq. (1).

The dimensionless potential $\mathcal{V}(\rho)$ in Eq. (C2) displays two minima at $\pm\rho_0$, corresponding to the ground state positions of the classical particles. Close to these minima, the potential can be approximated by parabolas, and the molecule vibrates with a frequency $\Omega = \omega_0(2\mathcal{V}''(\rho_0))^{1/2}$, where $\mathcal{V}''(z)$ is the second derivative with respect to z. Tunneling processes between $\pm\rho_0$ give rise to a splitting of these two levels, which we can identify as the exchange coupling. At the semiclassical level, we can thus estimate J as the tunneling amplitude [1]

$$J \approx \frac{\hbar\,\Omega}{\pi}\, e^{-\int_{-A}^{A} d\rho\,\sqrt{\mathcal{V}(\rho)-(\Omega/2\omega_0)}}, \tag{C4}$$

with A denoting the classical turning-point determined by the equation $\mathcal{V}(A) = \Omega/2\omega_0$. Alternatively, we can determine the spectrum of Eq. (C2) numerically, and extract the ground state splitting from there.

Figure 10 displays a comparison of the results of these two approaches as a function of $\tilde{r}_s$ for a nanotube of radius $R = 2$ nm in a confining potential of frequency $\hbar\omega_0 = 7.8$ meV. Both approaches yield an exponential decay of J with increasing $\tilde{r}_s$. The semiclassical method slightly overestimates the exchange coupling, but it gives a surprisingly accurate estimate for J. For a simple Coulomb interaction between

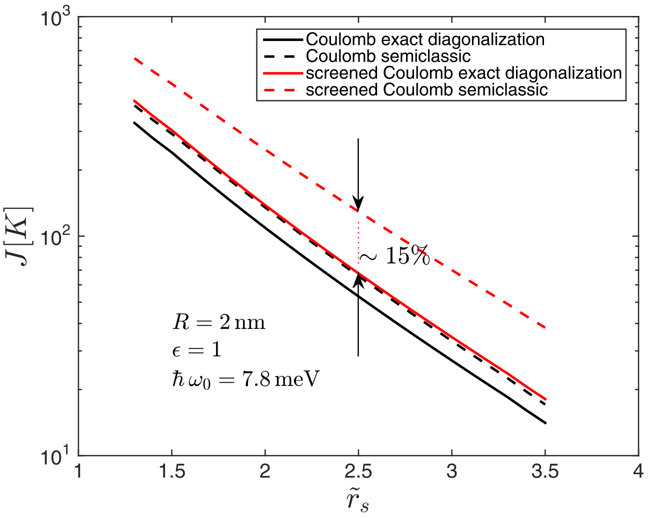

FIG. 10. The exchange interaction as function of the dimensionless ratio $\tilde{r}_s$ for a Wigner molecule. The radius of the nanotube was fixed to $R = 2$ nm and the confinement energy is $\hbar\,\omega_0 = 7.8$ meV. The solid lines are obtained using the pure Coulomb interaction (B4) while for the dashed lines the effective potential in Eq. (B2) with $\bar{\alpha} = 0$ has been used.

---

[8] For an infinite chain, we have $V^{(1)}(0) \to \infty$, a divergence compensated by the background of positive charges.

the two electrons, (B4), it estimates J's within $\sim 5\%$, but its accuracy remains around $\sim 15\,\%$ for the more appropriate nanotube interaction, Eq. (B2), too.

APPENDIX D: CHARGING ENERGY OF CARBON NANOTUBE IN A CONFINING POTENTIAL

The Coulomb energy of a nanoscale object often depends approximately quadratically on the number of charged particles,

$$E_{\mathrm{Coulomb}} \approx \frac{U}{2} N(N-1)\ . \tag{D1}$$

The charging energy U can be directly extracted from the Coulomb diamonds. The data presented in Ref. [25], e.g., yield a value $U \simeq 10$–12 meV.

In this appendix, we determine the effective value of U as a function of the particle number N for a CNT confined by a harmonic potential. Starting from the ansatz (D1), the value of U can be identified as the difference in the energy needed to add two consecutive electrons [44],

$$U \approx U_N \equiv \Delta E_{N+1} - \Delta E_N, \tag{D2}$$

with $\Delta E_N = E_{N+1} - E_N$, and E_N the total energy of the CNT with N confined charges.

In a parabolic confinement, the energy $E(\{z_i\})$ of a given classical charge configuration is the sum of the harmonic potential and the Coulomb energy,

$$E(\{z_i\}) = \sum_{i=1}^{N} \frac{\alpha}{2} z_i^2 + \sum_{i<j} \frac{e^2}{\epsilon |z_i - z_j|}. \tag{D3}$$

For each N, we first determine the coordinates z_i of the particles by minimizing Eq. (D3), and then compute the total energy E_N. Introducing the dimensionless coordinates $\zeta_i = z_i/l$, with $l = (e^2/\alpha\epsilon)^{1/3}$, the potential energy becomes

$$E_N = \mathcal{E}\left(\frac{1}{2}\sum_{i=1}^{N} \zeta_i^2 + \sum_{i<j} \frac{1}{|\zeta_i - \zeta_j|}\right). \tag{D4}$$

with the characteristic energy scale

$$\mathcal{E} = (e^4\alpha/\epsilon^2)^{1/3}.$$

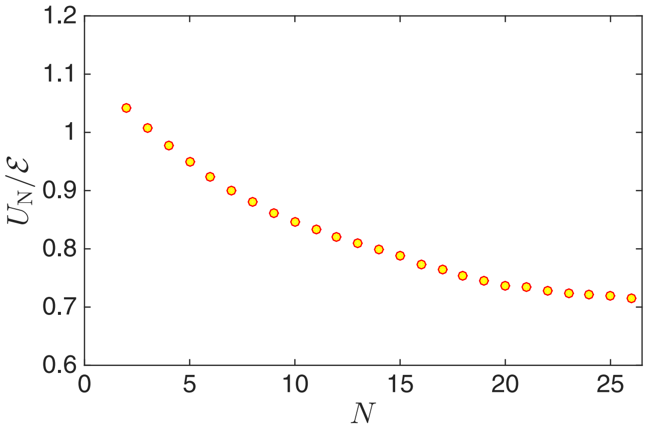

FIG. 11. Dimensionless charging energy as function of the particle number N.

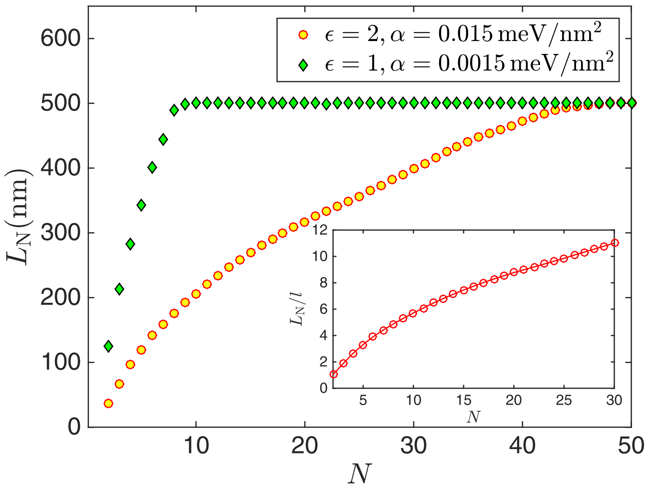

FIG. 12. The "length" of the Wigner crystal L_N, as a function of the number of charges N, for various potential depths α and dielectric constants. The length of the nanotube is $L = 500$ nm. (Inset) L_N/l for an infinite nanotube with parabolic confinement. L_N/l is a universal function of N.

As a consequence, U_N can be expressed as $U_N = \mathcal{E} f(N)$. We determined the universal function $f(N)$ numerically, and displayed it in Fig. 11. It has a weak dependence on N, and for particle numbers of interest $f(N) \approx 0.75$, yielding the relation

$$U^{\mathrm{eff}} \approx 0.75 \times \mathcal{E}.$$

This equation allows us to relate the screening parameter ϵ and the confinement parameter α through the experimentally determined charging energy. For $\epsilon = 2$, used throughout this work, $\alpha = 0.015$ meV/nm^2 yield $U^{\mathrm{eff}} \approx 14.7$ meV, roughly consistent with the data. For $\epsilon = 1$, however, one needs to use a much shallower confining potential with $\alpha \approx 0.0015$ meV/nm^2 in order to be consistent with the experimentally observed charging energy.

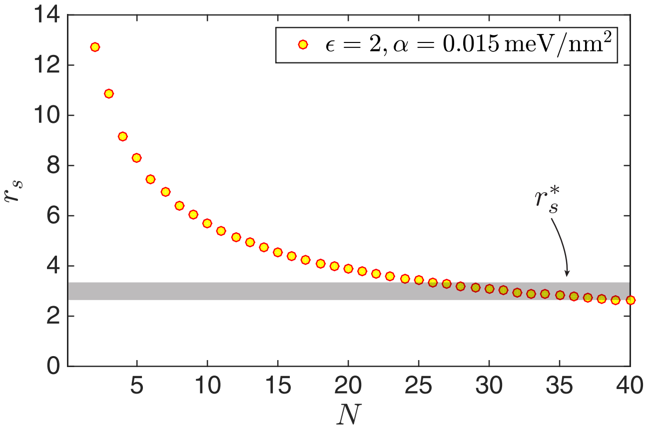

FIG. 13. The dimensionless parameter r_s as a function of the number of charges N in the middle of a 500 nm long nanotube for $\alpha = 0.015$ meV/nm^2 and $\epsilon = 2$. The Wigner crystal starts to melt at the center for $N = 26$, once r_s decreases below the crossover value $r_s^* \approx 3.3$.

In a finite nanotube of size L, the "length" of the Wigner crystal L_N increases monotonously with N up to the size of the tube. In an infinite nanotube, the growth is universal and can be expressed as $L_N/l = g(N)$, with $g(N)$ an universal function that we determined numerically. It is represented in the inset of Fig. 12. In the main panel of the same figure, we represent L_N as function of the number of charges N, for $\epsilon = 2$ and $\alpha \approx 0.015$ meV/nm^2 as well as for $\epsilon = 1$ and $\alpha \approx 0.0015$ meV/nm^2. While in the former case we can place about $N_{\max} \sim 40$ electrons on the nanotube before hitting the walls, in the 'unscreened' case, $\epsilon = 1$, this number is only $N_{\max} \sim 8$. Beyond this number the separation of the particles becomes quickly equidistant, yielding an almost uniform exchange coupling.

It is therefore evident that for large confinement potential depth α and strong screening ϵ a far larger number of charges can be squeezed inside the nanotube, as $l \propto (\alpha\,\epsilon)^{-1/3}$ decreases, but that is not a guarantee that the Wigner crystal state survive as N increases. The only relevant quantity that controls the melting point of the Wigner crystal is the dimensionless parameter r_s. As displayed in inset of Fig. 7, for a given configuration with N charges in the tube, r_s is site dependent and has the smallest value in the middle of the chain. In Fig. 13, we represent r_s in the middle of a 500-nm-long nanotube as function of the number of charges N. When only a few charges are confined to the nanotube, the gas is diluted and, as expected, $r_s \gg r^*_{1D}$, but as the charges accumulate, r_s decreases monotonously, and at some critical occupation $N_{\text{crit}} \approx 26$ it reaches r^*_{1D}, and the crystal starts to melt in the middle. Adding more charges, r_s decreases further, and the melting progresses towards the sides of the chain.

---

[1] K. A. Matveev, Phys. Rev. Lett. **92**, 106801 (2004).
[2] E. Wigner, Phys. Rev. **46**, 1002 (1934).
[3] L. Bonsall and A. A. Maradudin, Phys. Rev. B **15**, 1959 (1977).
[4] L. Cândido, B. Bernu, and D. M. Ceperley, Phys. Rev. B **70**, 094413 (2004).
[5] F. M. Peeters, Phys. Rev. B **30**, 159 (1984).
[6] A. V. Filinov, M. Bonitz, and Y. E. Lozovik, Phys. Rev. Lett. **86**, 3851 (2001).
[7] V. J. Goldman, M. Santos, M. Shayegan, and J. E. Cunningham, Phys. Rev. Lett. **65**, 2189 (1990).
[8] S. Chakravarty, S. Kivelson, C. Nayak, and K. Voelker, Philos. Mag. Part B **79**, 859 (1999).
[9] C. C. Grimes and G. Adams, Phys. Rev. Lett. **42**, 795 (1979).
[10] R. Egger, Phys. Rev. Lett. **82**, 3320 (1999).
[11] C. Yannouleas and U. Landman, Rep. Prog. Phys. **70**, 2067 (2007).
[12] H. J. Schulz, Phys. Rev. Lett. **71**, 1864 (1993).
[13] J. S. Meyer and K. A. Matveev, J. Phys.: Condens. Matter **21**, 023203 (2009).
[14] G. Piacente, I. V. Schweigert, J. J. Betouras, and F. M. Peeters, Phys. Rev. B **69**, 045324 (2004).
[15] A. Secchi and M. Rontani, Phys. Rev. B **80**, 041404 (2009).
[16] B. Wunsch, Phys. Rev. B **79**, 235408 (2009).
[17] A. Secchi and M. Rontani, Phys. Rev. B **82**, 035417 (2010).
[18] N. Traverso Ziani, F. Cavaliere, and M. Sassetti, Phys. Rev. B **86**, 125451 (2012).
[19] I. Kylänpää, F. Cavaliere, N. T. Ziani, M. Sassetti, and E. Räsänen, Phys. Rev. B **94**, 115417 (2016).
[20] M. Roy and P. Maksym, Physica E **42**, 771 (2010).
[21] M. Roy and P. A. Maksym, Phys. Rev. B **85**, 205432 (2012).
[22] L. I. Glazman, I. M. Ruzin, and B. I. Shklovskii, Phys. Rev. B **45**, 8454 (1992).
[23] K. A. Guerrero-Becerra and M. Rontani, Phys. Rev. B **90**, 125446 (2014).
[24] Y. Li, C. Yannouleas, and U. Landman, Phys. Rev. B **76**, 245310 (2007).
[25] V. V. Deshpande and M. Bockrath, Nat. Phys. **4**, 314 (2008).
[26] A gap in a nanotube can be induced by strain and curvature [43], too, but the relatively large gap reported in Ref. [25] is most likely due to confinement.
[27] S. Pecker, F. Kuemmeth, A. Secchi, M. Rontani, D. Ralph, P. McEuen, and S. Ilani, Nat. Phys. **9**, 576 (2013).
[28] M. Yamamoto, M. Stopa, Y. Tokura, Y. Hirayama, and S. Tarucha, Science **313**, 204 (2006).
[29] W. K. Hew, K. J. Thomas, M. Pepper, I. Farrer, D. Anderson, G. A. C. Jones, and D. A. Ritchie, Phys. Rev. Lett. **102**, 056804 (2009).
[30] M. Yamamoto, H. Takagi, M. Stopa, and S. Tarucha, Phys. Rev. B **85**, 041308 (2012).
[31] U. Meirav, M. A. Kastner, M. Heiblum, and S. J. Wind, Phys. Rev. B **40**, 5871 (1989).
[32] A. N. Aleshin, H. J. Lee, Y. W. Park, and K. Akagi, Phys. Rev. Lett. **93**, 196601 (2004).
[33] T. Giamarchi, *Quantum Physics in One Dimension* (Oxford University Press, Oxford, 2003).
[34] L. S. Levitov and A. M. Tsvelik, Phys. Rev. Lett. **90**, 016401 (2003).
[35] V. V. Deshpande, M. Bockrath, L. I. Glazman, and A. Yacoby, Nature (London) **464**, 209 (2010).
[36] B. Sutherland, Phys. Rev. B **12**, 3795 (1975).
[37] Y. Q. Li, M. Ma, D. N. Shi, and F. C. Zhang, Phys. Rev. Lett. **81**, 3527 (1998).
[38] T. Ando, J. Phys. Soc. Jpn. **69**, 1757 (2000).
[39] D. Huertas-Hernando, F. Guinea, and A. Brataas, Phys. Rev. B **74**, 155426 (2006).
[40] T. S. Jespersen, K. Grove-Rasmussen, J. Paaske, K. Muraki, T. Fujisawa, J. Nygård, and K. Flensberg, Nat. Phys. **7**, 348 (2011).
[41] F. Kuemmeth, S. Ilani, D. Ralph, and P. McEuen, Nature (London) **452**, 448 (2008).
[42] D. V. Bulaev, B. Trauzettel, and D. Loss, Phys. Rev. B **77**, 235301 (2008).
[43] E. A. Laird, F. Kuemmeth, G. A. Steele, K. Grove-Rasmussen, J. Nygård, K. Flensberg, and L. P. Kouwenhoven, Rev. Mod. Phys. **87**, 703 (2015).
[44] S. Sapmaz, P. Jarillo-Herrero, L. P. Kouwenhoven, and H. S. J. van der Zant, Semicond. Sci. Technol. **21**, S52 (2006).
[45] B. Kozinsky and N. Marzari, Phys. Rev. Lett. **96**, 166801 (2006).
[46] Y. Miyauchi, R. Saito, K. Sato, Y. Ohno, S. Iwasaki, T. Mizutani, J. Jiang, and S. Maruyama, Chem. Phys. Lett. **442**, 394 (2007).

[47] F. Guinea, M. Katsnelson, and A. Geim, Nat. Phys. **6**, 30 (2010).
[48] In suspended nanotubes charge distributions seem to be consistent with $\epsilon \approx 1$ [S. Ilani (private communication)].
[49] Y. Oreg, K. Byczuk, and B. I. Halperin, Phys. Rev. Lett. **85**, 365 (2000).
[50] J. Paaske, A. Rosch, P. Wolfle, N. Mason, C. M. Marcus, and J. Nygard, Nat. Phys. **2**, 460 (2006).
[51] C. Schenke, S. Koller, L. Mayrhofer, and M. Grifoni, Phys. Rev. B **80**, 035412 (2009).
[52] W. Häusler, Z. Physik B Cond. Matt. **99**, 551 (1995).
[53] K. A. Matveev, Phys. Rev. B **70**, 245319 (2004).
[54] Y. Homma, S. Chiashi, and Y. Kobayashi, Rep. Prog. Phys. **72**, 066502 (2009).
[55] Multiparticle exchanges considered in Ref. [66] are expected to give a small correction only, and shall be neglected here.
[56] C. P. Moca *et al.* (unpublished).
[57] G. Zarand, A. Brataas, and D. Goldhaber-Gordon, Solid State Commun. **126**, 463 (2003).
[58] P. Jarillo-Herrero, J. Kong, H. S. J. van der Zant, C. Dekker, L. P. Kouwenhoven, and S. De Franceschi, Nature **434**, 484 (2005).
[59] A. W. Ludwig and I. Affleck, Nucl. Phys. B **428**, 545 (1994).
[60] A. Auerbach, *Interacting Electrons and Quantum Magnetism*, Graduate Texts in Contemporary Physics (Springer-Verlag, New York, 1994).
[61] D. R. Schmid, S. Smirnov, M. Margańska, A. Dirnaichner, P. L. Stiller, M. Grifoni, A. K. Hüttel, and C. Strunk, Phys. Rev. B **91**, 155435 (2015).
[62] T. Ando, J. Phys. Soc. Jpn. **74**, 777 (2005).
[63] I. Gradshteyn and I. Ryzhik, *Table of Integrals, Series, and Products (Corrected and Enlarged Edition)* (Academic Press, San-Diego, CA, 1980).
[64] J. Levinsen, P. Massignan, G. M. Bruun, and M. M. Parish, Sci. Adv. **1**, e1500197 (2015).
[65] C. Yannouleas, B. B. Brandt, and U. Landman, New J. Phys. **18**, 073018 (2016).
[66] A. D. Klironomos, R. R. Ramazashvili, and K. A. Matveev, Phys. Rev. B **72**, 195343 (2005).